

Recent Development of Plasmonic Metallic Subwavelength Structures: A Review

Yongqi Fu^{1,*} and Yong Yang²

¹*School of Physical Electronics, University of Electronic Science and Technology of China, Chengdu 610054, P. R. China*

²*Institute of Optics and Electronics, Chinese Academy of Sciences, Shuangliu, P.O. Box 350, Chengdu 610209, P. R. China*

As a literature review, a recent development of plasmonic metallic subwavelength structures is presented in this paper. Total three topics are addressed: (1) Plasmonic structures for imaging and superfocusing; (2) Plasmonic structures for antenna; and (3) Metallic nanoparticles array for biosensing. Design of the plasmonic devices is illustrated in detail. In addition, fabrications and applications are briefly introduced so as to keep integrality of this paper.

Keywords: Plasmonic Structures, Imaging, Superfocusing, Antenna, Biosensing.

CONTENTS

1. Introduction	1412
2. Plasmonic Structures for Imaging and Superfocusing	1412
2.1. Depth Tuned Method	1413
2.2. Width Tuned Method	1415
2.3. Plasmonic Structures with Variant Periods	1416
2.4. Funnel-Shaped Array for Superfocusing	1420
3. Plasmonic Structures for Antenna	1421
3.1. Electromagnetic Band-Gap Structures-Based Antennas	1421
3.2. Waveguide Slit Array Antenna	1422
4. Metallic Nanoparticles Array for Biosensing	1423
4.1. Design Methods	1423
4.2. Nanofabrication	1427
5. Summary	1428
Acknowledgment	1429
References	1429

1. INTRODUCTION

In recent years, a flurry of activity in the fundamental research and development of surface plasmon based structures and devices were reported.^{1–6} Surface plasmons are collective charge oscillations that occur at the interface between conductors and dielectrics. They can take various forms, ranging from freely propagating electron density waves along metal surfaces to localized electron oscillations on metal nanoparticles. Their unique properties enable a wide range of practical applications, including light guiding and manipulation at the nanoscale,⁷ optical filtering,⁸ bio-detection at the single

molecule level,⁹ enhanced optical transmission through subwavelength apertures,¹ and high resolution optical imaging below the diffraction limit.¹⁰

In this paper, a literature review is given for the purpose of displaying a physical picture of nanophotonic devices design for the relevant readers. Firstly, the plasmonic structures for imaging and superfocusing are presented. Then the plasmonic structure-based antennas are introduced. Finally, a detailed description regarding metallic nanoparticles array for biosensing is given. Considering scope of this journal, we mainly focus on the design issues of the plasmonic structures.

2. PLASMONIC STRUCTURES FOR IMAGING AND SUPERFOCUSING

Superlens as a type of nanolens with imaging resolution beyond diffraction limit was firstly reported by Zahang et al.^{10–13} It was designed on the basis of negative refractive index (NFI) materials (also named “metamaterials”). Considering fabrication limitation of the metamaterials for the optical systems working at visible wavelength, an approximate metamaterial: Ag thin film was employed to replace the ideal NFI materials. A sandwiched PMMA-Ag-photoresist structure was designed to realize superfocusing. However, there is no working distance between the superlens and object plane and amplifying function. Therefore, another superlens they called “hyperlens” was presented.¹⁴ It can produce amplified image by the hyperlens composed of alternative dielectric-Ag

*Author to whom correspondence should be addressed.

multilayers structured in parabolic shape. But there is still no working distance. The object with etched letters of "NANO" is tightly attached with the hyperlens together. Moreover, essentially, both the superlens and hyperlens can function as one-dimensional imaging only because the object of "NANO" consists of single lines instead of two-dimensional patterns. Thus it is still not an engineered optical lens. Considering this, plasmonic metallic structures flanked with subwavelength corrugations/grooves/nanoslits were explored. They can realize beaming, imaging and superfocusing by means of phase modulation near-field interference. Here two methods of phase modulation were introduced: (1) depth tuning; and (2) width tuning. After that, Zone plate-like microstructures and a funnel-shaped array for superfocusing were presented.

2.1. Depth Tuned Method

Figure 1 illustrates a typical slit-groove-based focusing structure, which was formed by a single subwavelength metallic slit surrounded by a finite array of grooves at the output surface. When the TM polarized light is launched in the slit from the left side, it couples to SPPs in the metallic slit and then is diffracted to the output surface as well as the forward region in the air. The diffracted light wave on the output surface will propagate along the silver-air interface and scatter into radiation light at the groove

region with specific phase and amplitude. The interference of the light emerging from the slit and grooves will create a focus at the point where the values of phase difference between the emissions are the integer multiples of 2π . Thus, the relative phase profile distribution at the output surface basically determines the focus position.¹⁵

The SPPs wave is a special kind of electromagnetic field, which can propagate along the metallic surfaces while keep bounded near the surface without radiating away. Considering two closely placed parallel metallic plates, the SPPs of each surface will be coupled and propagate in the form of a waveguide mode, mainly for TM polarized set (E_x , H_y , and E_z). The dispersion relation between the effective refractive index and slit depth implies a potential way of phase modulation by simply tuning the slit depth. When TM polarized incident plane wave impinges the slit entrance, it will excite SPPs. Then the SPPs couples with the incident wave and propagates along the slits region until it reaches the exit where the coupled wave radiates into the beam in free space. The phase of light ϕ transmitted through the nanoslits can be expressed as

$$\phi = \phi_{01} + \phi_{12} + n_1 k h(x) - \theta \quad (1)$$

The last term θ , originating from the multiple reflections between the entrance and exit interfaces, can be calculated with the following equation

$$\theta = \arg(1 + \rho_{01}\rho_{12}e^{i2kh(x)}) \quad (2)$$



Yongqi Fu was born in P. R. China. He received his B.Eng, M.S, and Ph.D. in mechanical engineering from Jilin University of Technology, Changchun Institute of Optics and Fine Mechanics, and the Chinese Academy of Sciences in 1988, 1994, and 1996, respectively. He worked in the State Key Laboratory of Applied Optics from 1996 to 1998 as a Postdoctoral Fellow. He then worked in the Precision Engineering and Nanotechnology (PEN) Center as a Research Fellow from August 1998 to September 2007. He is the leader of the FIB group in PEN Center. Currently, he works at School of Physical Electronics, University of Electronic Science and Technology of China as professor in nanophotonics. His current research direction is micro/nanofabrication, applications of FIB in microelectronics/semiconductors, nano-photonics, MOEMS/NEMS, micro/nano-optics, fiber optics, optical measurement/nanometrology, and optical system instrumentation, e.g., nano-inspection/detection system. He is the first author of more than 90 referred journal papers. For more information about the author, please visit his personnel homepage with the following website address: <http://www.ntu.edu.sg/home/yqfu/fyqpage.htm>.



Yong Yang is a doctor student in the Institute of Optics and Electronics of CAS in China. He received his BS degree from Dalian Maritime University in 1999 and MS degree from Chongqing University in 2005, respectively. After graduation from DMU, he worked as an engineer in Neptune Orient Lines of Singapore. He is currently majored in optical lithography, optical measurement and optical control. His research interests also include MEMS applied in medical field.

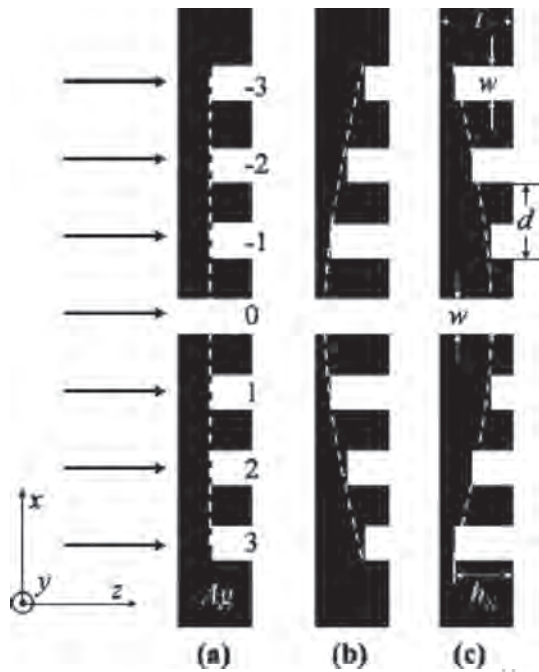


Fig. 1. Schematic view of the structures formed by a single subwavelength slit surrounded by grooves with traced depth profile. t denotes the thickness of silver film, w denotes the width of the slit and all grooves, d denotes the groove period, and hN denotes the depth of grooves with the serial number of N . kd denotes the depth difference between the adjacent grooves, and $kd = 0$, $kd < 0$, $kd > 0$ represent the cases shown in (a), (b), and (c), respectively. Reprinted with permission from [15], H. Shi et al., *Appl. Phys. Lett.* 91, 093111 (2007). © 2007, American Institute of Physics.

where \mathbf{k} is the wave vector of the light in dielectric/Ag interface, and $h(x)$ the slit depth. Subscripts 0, 1, 2 denote the media before, inside, and after the nanoslit array, respectively. The dispersion relation between the effective refractive index and slit width implies a potential way of phase modulation by simply tuning the slit depth. The wave vector \mathbf{k} for the coupled surface plasmons in the interface can be expressed as

$$\mathbf{k} = k_0 \left[1 + \frac{1}{2} \eta^2 \left(1 + \sqrt{1 + \frac{4}{\eta^2} (1 + |\varepsilon|)} \right) \right] \quad (3)$$

where $\eta = 2/(k_0 w |\varepsilon|)$, w is the width of slit defined in the structure, and $\varepsilon = \varepsilon_m \varepsilon_d / \varepsilon_m + \varepsilon_d$.

Our target is that design a nanostructure which can act as a “nano-lens” to realize beam shaping such as collimation or focusing for the future possible usage of detection and inspection. A higher spatial resolution can be expected through this type of lens. Figure 1 is our design enhanced SPPs-based nanostructure, which consists of 7 slits. The central slit is thoroughly penetrated through the Ag thin film. Depth distribution of the other 6 slits is symmetrical to the central slit, and gradually decreases. The outline of the groove bottom is designed being a curve of parabolic. Beam shaping can be realized theoretically by a

way of controlling phase distribution along one direction. Required phase distribution of the emitted light at position x can be derived readily according to the equal optical path length principle

$$\phi(x) = \frac{2m\pi}{\lambda} h(x) = 2m\pi + \frac{2\pi f}{\lambda} - \frac{2\pi\sqrt{f^2 + x^2}}{\lambda} \quad (4)$$

where m is an arbitrary integer number, and f the focal length of the probe which is a function of slit width, period, metal thickness, and depth distribution curve as $f = f(a, \Lambda, h, d(x))$. The corresponding phase delay due to the modulated depth with the standard parabolic function $d(x) = ax^2 + bx + c$ causes redistribution of the peak transmission and convergence of the coupled SP wave in the grooves by which the beam is shaped. Considering fabrication possibility, we discretized the continuous phase distribution into 7 steps and transferred them into 7 corresponding slits with different depth. Period and width of the slits are 500 nm and 200 nm, respectively. Incident wavelength and excited SPPs wavelength is $\lambda_{in} = 527$ nm (for white light source), and $\lambda_{SP} = 525$ nm, respectively. The nanostructure will be fabricated on the Ag thin film coated on the quartz substrate with thickness of 200 nm.

Calculated E_x relative phase distribution profiles at groove regions along the x -axis at the output surface is shown in Figure 2(a). The circle marks denote the data of the control structure with $kd = 0$, and the square and triangle marks denote the data of the structure with $kd = -50$ nm and $kd = 50$ nm, respectively. Obviously, the curvature of the relative phase profile at the output surface varies with the groove depth distribution profile as expected; the deeper the groove depth the larger the relative phase value. Figures 2(b)–(d) illustrate the corresponding $|H_y|^2$ intensity distributions for the cases shown in Figures 1(a)–(c). The $|H_y|^2$ intensity distribution results show that the energy emerging from the structure overlaps the axis within several microns, concentrating most of the energy in an extremely small region. For example, the flat groove depth trace case shown in Figure 2(b) reveals the focal length of 1.49 μm and the full width at half maximum (FWHM) of the focal width of 0.62 μm , i.e., focal spot smaller than a wavelength. If the groove depth trace is designed to spatially decrease with their distance from the central slit with $kd = -50$ nm, the focal length will reduce to 1.22 μm with the decreased focal width of 0.55 μm . On the contrary, the groove depth trace with $kd = 50$ nm shows a contrary performance with the increased focal length of 1.99 μm and focal width of 0.67 μm . The focal length of the slit-groove-based focusing structures can be adjusted in certain value if the groove depths are arranged in traced profile. With the regulation of the groove depth profile, it is possible to modify the focus position in the precision of nanoscale without increasing the size of the nanodevice.

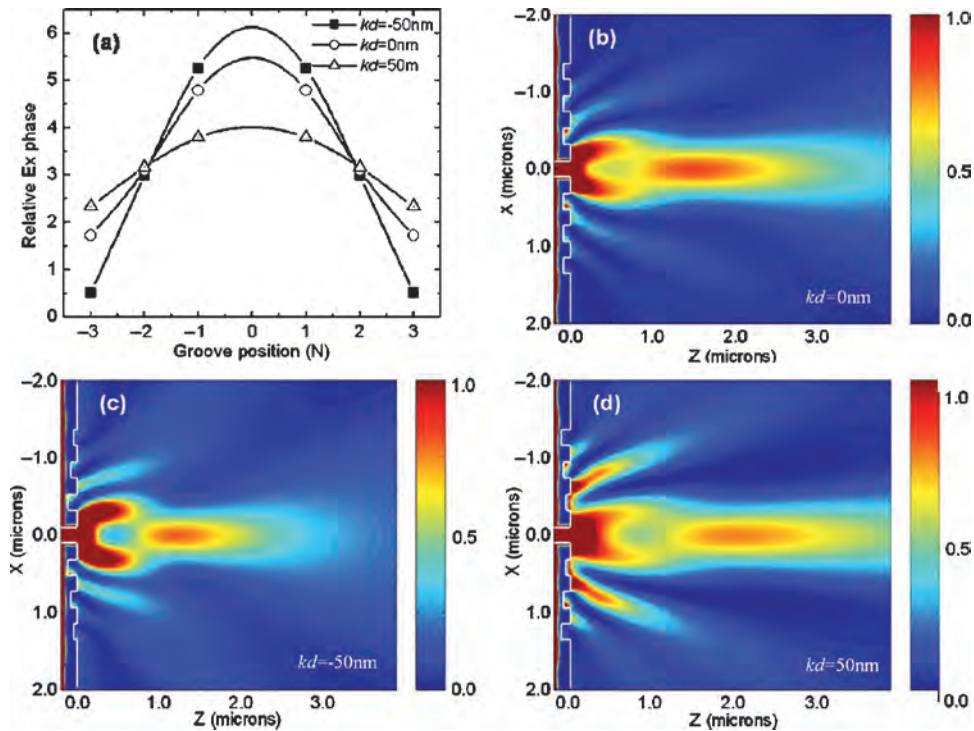


Fig. 2. FDTD simulation results for modulating the focal length with trace profiles. (a) Relative phase E_x distributions for the three depth trace profiles shown in Figure 1(b) $|H_y|^2$ distributions for the cases shown in Figure 1(a) with $kd = 0$, (c) $|H_y|^2$ distributions for the cases shown in Figure 1(b) with $kd = -50$ nm, and (d) $|H_y|^2$ distributions for the cases shown in Figure 1(a) with $kd = 50$ nm. The other parameters are set as $t = 200$ nm, $w = 200$ nm, and $d = 420$ nm. Reprinted with permission from [15], H. Shi et al., *Appl. Phys. Lett.* 91, 093111 (2007). © 2007, American Institute of Physics.

2.2. Width Tuned Method

A novel method is proposed to manipulate beam by modulating light phase through a metallic film with arrayed nano-slits, which have constant depth but variant widths.^{16,17} The slits transport electro-magnetic energy in the form of surface plasmon polaritons (SPPs) in nano-metric waveguides and provide desired phase retardations of beam manipulating with variant phase propagation constant.

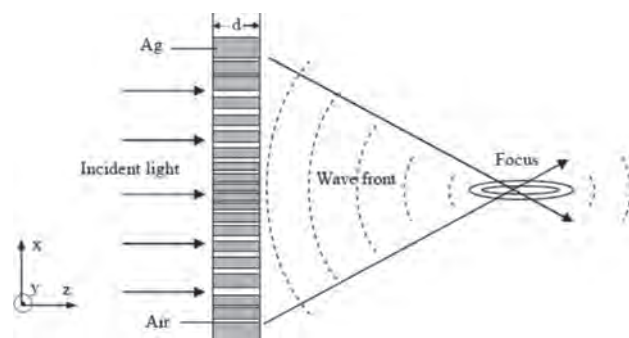


Fig. 3. A schematic of a nano-slit array with different width formed on thin metallic film. Metal thickness in this configuration is d , and each slit width is determined for required phase distribution on the exit side, respectively. A TM-polarized plane wave (consists of E_x , H_y and E_z field component, and H_y component parallel to the y -axis) is incident to the slit array from the left side. Reprinted with permission from [16], H. Shi et al., *Opt. Express* 13, 6815 (2005). © 2005, Optical Society of American.

To illustrate the above idea of modulating phase, a metallic nano-slits lens is designed. The parameters of the lens are as follows: $D = 4 \mu\text{m}$, $f = 0.6 \mu\text{m}$, $\lambda = 0.65 \mu\text{m}$, $d = 0.5 \mu\text{m}$, where D is the diameter of the lens aperture, f the focus length, λ the wavelength and d the thickness of the film. The two sides of the lens is air. The schematic of lens is given in Figure 3, where a metallic film is perforated with a great number of nano-slits with specifically designed widths and transmitted light from slits is modulated and converges in free space. The required phase distribution of emitted light at position x can be obtained readily according to the equal optical length principle where n is an arbitrary integer number.

$$\phi(x) = 2n\pi + \frac{2\pi f}{\lambda} - \frac{2\pi\sqrt{f^2 + x^2}}{\lambda} \quad (5)$$

After FDTD calculation, the resulting Poynting vector is obtained and showed in Figure 4(a). A clear-cut focus appears about 0.6 micron away from the exit surface, which agrees with our design. The cross section of focus spot in x direction is given in Figure 4(b), indicating a full-width at half-maximum (FWHM) of 270 nm. The extraordinary light transmission effect of SPPs through sub-wavelength slits is also observed in the simulation with a transmission enhance factor of about 1.8 times.

Another application of the width tuning is design beam deflector on the basis of SPPs wave effect.¹⁸ The nanoslits with different width and depth can lead to different phase

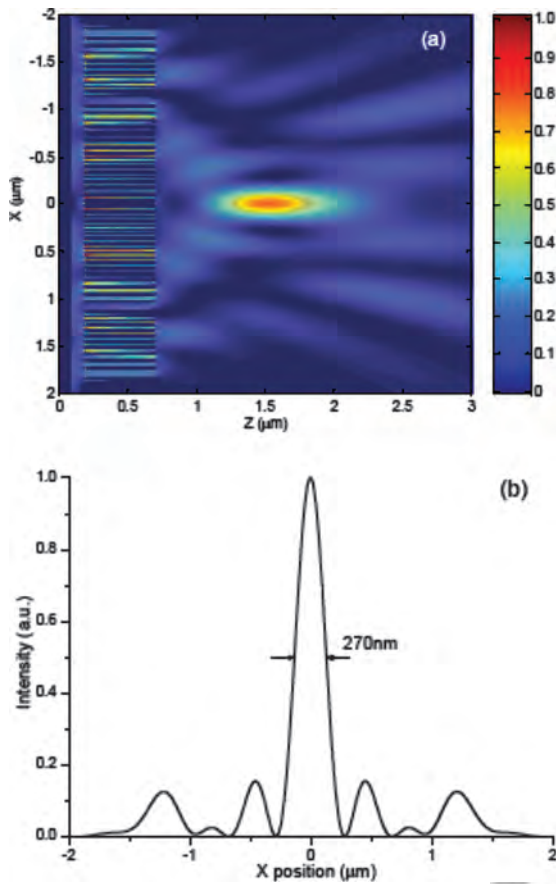


Fig. 4. (a) FDTD calculated result of normalized Poynting Vector S_z for designed metallic nano-slits lens. Film thickness is 500 nm, and the total slits number is 65. The structure's exit side is positioned at $z = 0.7 \mu\text{m}$. (b) Cross section of the focus at $z = 1.5 \mu\text{m}$. Reprinted with permission from [16], H. Shi et al., *Opt. Express* 13, 6815 (2005). © 2005, Optical Society of American.

retardations while the surface plasmons passing through the structure. A beam splitting effect with the splitting angle of near 90° can be achieved by adjusting the width and depth of the slits accordingly. The splitting angle can be modulated precisely from 0° to $\sim 90^\circ$ by changing the position and width of each nanoslit. The structure, with its miniaturized size, can be applied in the fields like optical control, optical switch, imaging, and micro-mechanical-electronic-systems (MEMS) etc.

Considering the surface plasmon mode in metallic grooves for true metals, Shi et al. proposed a revised version of the analytical and numerical model on the light diffraction from a subwavelength slit surrounded by finite number grooves on a metallic film.¹⁹ The revised model indicates that the optical property of true metals, even for good metals such as Ag and Au, may possess great influence to the light diffraction as the size of subwavelength structure is comparable to the depth of light penetration into metal.

In summary, the modulation ability is limited to a certain extent by means of either pure depth tuning or width

tuning only. Combination of both tuning method together is more effective for the purpose of superfocusing and imaging.

2.3. Plasmonic Structures with Variant Periods

A new super lens, plasmonic micro-zone plate-like (PMZP) structure was put forth.^{20,21} It is different from the concept of metamaterials-based superlens reported by Zhang.¹² It can realize converting the enhanced SPP wave to propagating waves so as to increase the effective propagation distance. Liu et al. theoretically studied that diffractive elements may work at near-field in the scanning near-field optical microscope (SNOM) systems to replace the conventional optical fiber probes.¹³ But controlling constant working distance l ($l < \lambda/10$) between the planar diffractive element and sample surface is difficult in practice. Configuration of the PMZP is an asymmetric structure with variant periods in which a thin film of Ag is sandwiched between air and glass, see Figure 5. Unlike the conventional zone plates with metal film of Cr, Al, or Ni, our PMZP is a device that a quartz substrate coated with Ag thin film which is embedded with a zone plate structure with the zone number $N < 10$. For an evanescent wave with given k_x , we have $k_{zj} = +[\varepsilon_j(\omega/c)^2 - k_x^2]^{1/2}$ for $j = 1$ (air) and $j = 3$ (glass); and $k_{zj} = +i[k_x^2 - \varepsilon_j(\omega/c)^2]^{1/2}$ for $j = 2$ (Ag film). Superfocusing requires regenerating the evanescent waves. Thus the PMZP needs to be operated with the condition $|k_{z1}/\varepsilon_1 + k_{z2}/\varepsilon_2 \parallel k_{z2}/\varepsilon_2 + k_{z3}/\varepsilon_3| \rightarrow 0$. Physically, this would require exciting a surface plasmon at either the air or the glass side. For p -polarized light (SPP wave is excited for TM mode only), a negative permittivity is sufficient for focusing evanescent waves if the metal film thickness and object are much smaller than the

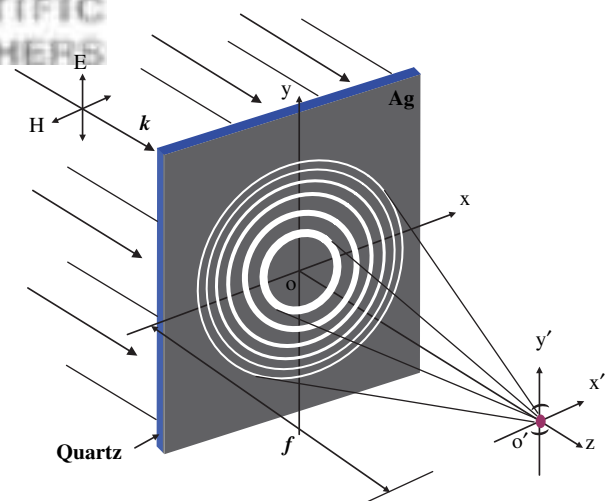


Fig. 5. Schematic of the plasmonic micro-zone plate super-focusing with focal length f . It is illuminated by a plane wave with 633 nm incident wavelength. The Ag film has permittivity $\varepsilon = -17.244 + 0.498i$ at $\lambda_0 = 633 \text{ nm}$. In our FDTD simulations the perfectly matched layer (PML) boundary condition was applied at the grid boundaries.

incident wavelength. Because electric permittivity $\varepsilon < 0$ occurs naturally in silver and other noble metals at visible wavelengths, a thin metallic film can act as an optical superlens. In the electrostatic limit, the p -polarized light,

dependence on permeability μ is eliminated and only permittivity ε is relevant.

The super lens can image at micron scale distance (around $\lambda \sim 5\lambda$, we call this range “quasi-far-field region.”

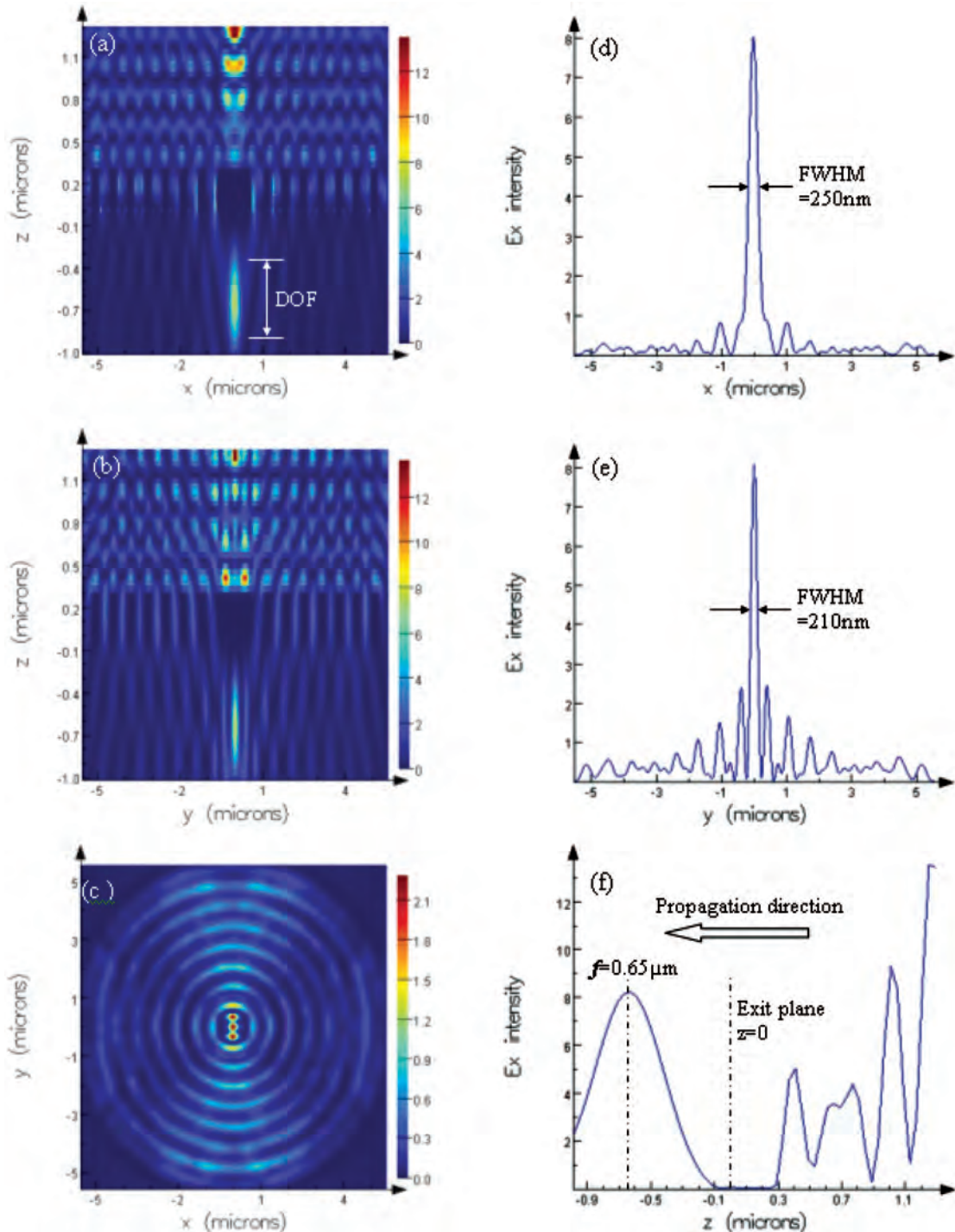


Fig. 6. An example of a plasmonic micro-zone plate (negative) with outer diameter, Ag film thickness, and working wavelength of $10.34 \mu\text{m}$, 300 nm , and 633 nm , respectively. Electric field distribution results calculated using FDTD algorithm. Propagation direction is z . Electric field E_x intensity in (a) x - z plane; (b) y - z plane; and (c) x - y plane. Electric field transmission in line $z = -0.65 \mu\text{m}$ (calculated focal plane) in (d) x - z plane, $y = 0$; (e) y - z plane, $x = 0$; and (f) x - y plane, $z = 0$. Designed focal length, outer diameter, and outermost zone width using scalar theory is $f = 0.5 \mu\text{m}$, $10.53 \mu\text{m}$ and 28 nm , respectively. Calculated depth of focus (DOF) is $\sim 500 \text{ nm}$ (scalar theory designed value is 2.58 nm). The site of $z = 0$ is the exit plane of the Ag film.

Both scalar theory and vector theory are applicable in this region.) along propagation direction. The conversion from SPP wave to propagation waves in the quasi-far-field region takes place by diffraction from the subwavelength zones of the PMZP. Focusing characteristics of the PMZP is quite different from the conventional Fresnel zone plates. The simulated focal length of our PMZP f_{PMZP} and depth of focus (DOF) are larger than that of the designed value using the classical equations: $DOF = \pm 2\Delta r^2/\lambda$, where $n = 1, 2, 3, \dots$, f_{FZP} is the designed principal focal length of Fresnel zone plates and given in terms of radius R of the inner ring and incident wavelength by $f_{\text{FZP}} = R^2/\lambda$, Δr is the outmost zone width, and λ is the incident wavelength. This phenomenon is apparent especially for the DOF, as shown in Figures 6(a) and (b), and Figure 7. It may attribute to the SPP wave coupling through the cavity mode and is involved for contribution of the beam focusing. The focusing is formed by interference between the SPP wave and the diffraction waves from the zones. The interference can exist within a coherence length L_c of the “source,” but not beyond it. The source equivalent to a source with central wavelength of $\lambda_{\text{in}} = 633$ nm, and bandwidth $\Delta\lambda = \lambda_{\text{in}} - \lambda_{\text{SP}}$, and thus $DOF \leq L_c$, where $L_c \approx \lambda^2/(\lambda_{\text{in}} - \lambda_{\text{SP}})$. For the SPP interference, the wave vector k_x of the incident optical wave projected on the plane parallel to the surface of the metal film must equal to k_{SP} .

Corresponding FDTD analysis results reveal that it has unique focusing performance of elongated focal length and DOF with a focused spot size beyond diffraction limit in comparison to the conventional zone plates. In addition, it can work at longer working distance ranging from

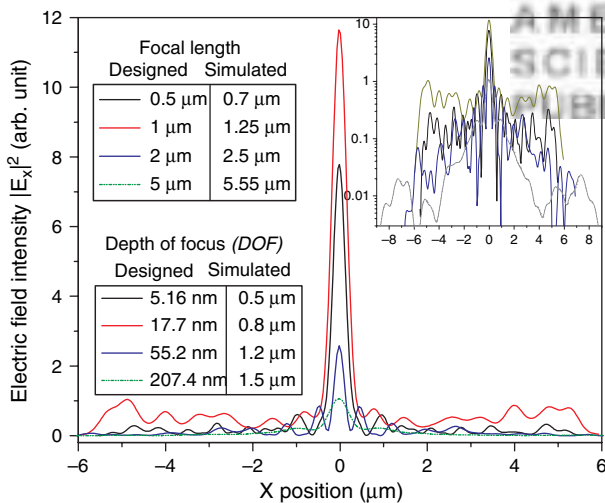


Fig. 7. Electric field intensity distribution $|E_x|^2$ versus x in focal planes for the PMZPs with four designed focal length. Simulated focal length and DOF are greatly larger than that of the designed values. Inset is the corresponding plot with logarithm scale in longitudinal axis. Corresponding beam spot size (FWHM) in x direction for the four designed focal length of 0.5 μm , 1 μm , 2 μm , and 5 μm is 250 nm, 370 nm, 280 nm, and 550 nm, respectively.

$\sim\lambda$ to 5λ or more that gives more flexibility for the relevant application systems working in this quasi-far-field region. This performance will be helpful for the PMZPs being used as optical probes for high resolution imaging and detection.

However, sidelobes for the previous PMZP structures are high. It occupies a lot of energy and degrades intensity of main lobe. To solve this problem, we put forth a nanostructure which is composed of pinholes with micron scale dimension and diameter smaller than $\lambda/2$, as shown in Figure 8.²² We refer to this structure as nanopinhole-based plasmonic structure (NPPS) and explore its application as “superlens.” Influence of the cut-off wavelength effect on propagation and transmission properties were analyzed for the purpose of revealing optical performance and physical picture of the structure in near-field region.

The proposed superlens is an asymmetric structure in which a thin film of Ag of 200 nm in thickness is sandwiched between air and quartz substrate. The pinholes with different diameters are uniformly and symmetrically distributed along the open subwavelength zones of a zone plate. It works at visible wavelength regime and propagates at near-field with the outer diameter $D < 15$ μm and zone number $N < 10$. The structure consists of 8 rings of pinholes with the following diameters (see inset pattern in Fig. 9(a)): 158 nm (8th ring), 177 nm (7th ring), 202 nm (6th ring), 234 nm (5th ring), 280 nm (4th ring), 349 nm (3rd ring), 467 nm (2nd ring), and 735 nm (1st ring). For the wavelength $\lambda_{\text{in}} = 633$ nm at normal incidence, the pinhole diameters at the outer four rings are less than $\lambda/2$. The total dimension of the structure is 12.07 μm . All the pinholes have a fixed ratio $K = d/w = 3.0$, where d is the

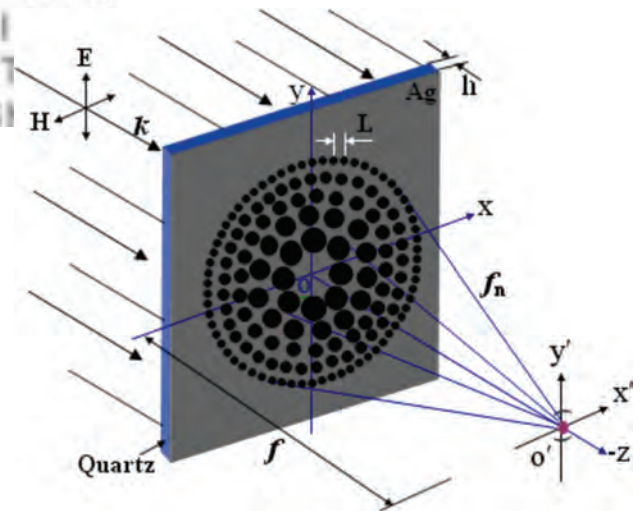


Fig. 8. Schematization of the pinhole array with focal length f . Lateral central distance L determines wave coupling between the neighbored holes. The pinholes are uniformly distributed along the zones. It is illuminated by a plane wave with 633 nm incident wavelength. The Ag film has permittivity $\varepsilon = -17.6235 + 0.4204i$ at $\lambda_0 = 633$ nm. In our FDTD simulations the perfectly matched layer (PML) boundary condition was applied at the grid boundaries.

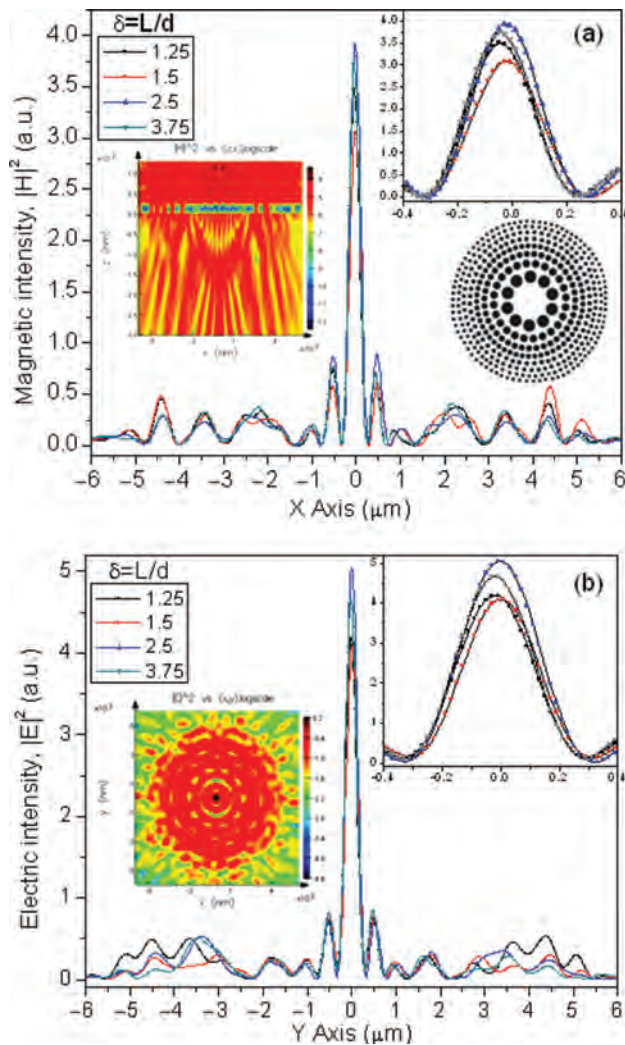


Fig. 9. Electromagnetic field analysis results for (a) E -field intensity $|E|^2$ distribution at y - z plane. Inset is 2D image of E -field intensity $|E|^2$ distribution at y - z plane. Inset image is $|E|^2$ distribution at x - y plane. (b) H -field intensity $|H|^2$ distribution at x - z plane. Inset is 2D image of H -field intensity $|H|^2$ distribution at x - z plane. Inset pattern is one of the pinhole structure with $\delta = d/L = 2.5$. Incident wavelength is 633 nm.

diameter of pinholes and w is the width of corresponding open zones in a zone plate. For the transmission with the SPPs excitation (E_{\perp} field), the electric intensity $|E|^2$ distribution at x - z plane and magnetic intensity $|H|^2$ distribution at y - z plane were calculated using the FDTD algorithm respectively, as shown in Figures 9(a) and (b). It can be seen that an apparent focal region is observed for both components $|H|^2$ and $|E|^2$. Spot size at full-width and half-maximum (FWHM) increases slightly with increase of the pinholes periodicity L . Sidelobes (± 1 orders) are significantly suppressed.

However, most of them were designed on the basis of Ag thin film metallic nanostructures. Corrosion-induced electrochemical damage on surface of the Ag film exists at ambient atmosphere, especially in the period of time

after micro/nanofabrication. The corrosion originates from oxidation and sulfuration which is well known for bulk Ag. But for the Ag thin film, dielectric constant of the Ag thin film will be definitely changed due to the oxidation and sulfuration. Optical performance of the nanophotonic devices varies accordingly. To overcome this problem, we put forth a hybrid Au–Ag subwavelength structures with Au thin film covered on the Ag film surface, as shown in Figure 10.^{24, 25} Therefore, the Au film acts as both a protector and modulator here. On the one hand, it can protect Ag film surface from oxidation. On the other hand, it can modulate beaming and propagation properties of the devices. But it is very tedious to study the Au film modulation here by experiments only due to complex thin film coating process required. Considering this, a theoretical study is carried out first by means of computational numerical calculations for the purpose of revealing physical picture of the hybrid Au–Ag film modulation in the subwavelength structures. A finite-difference and time-domain (FDTD) algorithm was adopted here for the computational calculation and numerical simulation. Corresponding calculation results further show that thickness of both the Au and Ag thin films has significant tailoring function due to their great contribution to superfocusing and transmission. Improved focusing performance and enhanced transmission can be obtained if h_{Au} and h_{Ag} match each other.

Currently, the FIBM technique is a commonly used approach to fabricate such nanostructures due to its unique advantages of one-step fabrication, nanoscale resolution, and no materials selectivity etc. However, the FIBM has its own problems too. Regarding the FIBM fabricated corrugations and subwavelength aperture, there are two issues have not been addressed at present: (1) V-shaped structuring effect; (2) variation of optical property of the

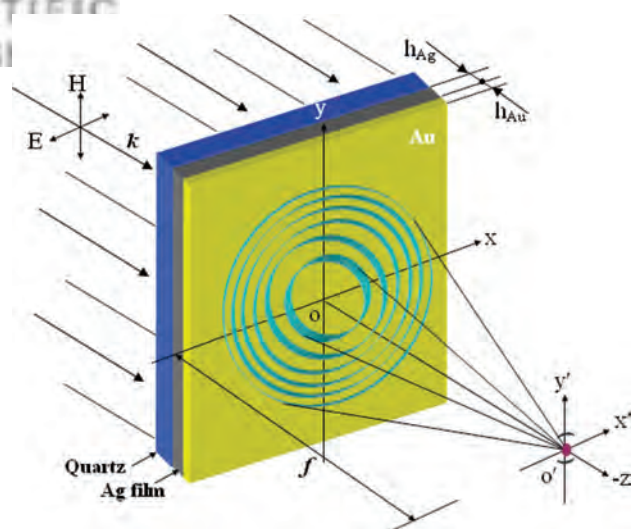


Fig. 10. Schematic of the plasmonic micro-zone plate super-focusing with focal length f . It is illuminated by a plane wave with 633 nm incident wavelength. In our FDTD simulations the perfectly matched layer (PML) boundary condition was applied at the grid boundaries.

metal film (optical property will be changed due to ion implantation of the Ga^+ after the FIBM²⁶). These two issues have not been answered in the existing theoretical works. The second issue will be further investigated via both theoretical and experimental study and reported in an individual paper later. This paper extends the prior works from theoretical study of the ideal rectangular-based corrugations to the practical nanofabrication-related issue: the V-shaped structuring effect during formation of the corrugations. In cross-section view of the FIBM fabricated structures, a V-shape instead of the ideal rectangular shape (rectangular grooves were assumed in all the previous reports which were cited in the reference) appears while mills the structures designed with high aspect ratio (depth to width), as shown in Figure 11.²⁷ For the designed nanostructures with rectangular shape in the cross-section view, a shape evolution from the designed rectangular to the “V” shape is unavoidable after the FIBM. Normally, geometrical characterization of the V-shaped nanostructures is carried out using an atomic force microscope (AFM) with tipping mode. However, it is too difficult to accurately measure the dimension of the nanostructures due to inherent shortages of the AFM. Therefore, it is too difficult to experimentally study and evaluate their influence on optical performance which is an important issue for designing the metallic nanostructures. Considering this, we addressed this problem, and analyzed the influence on the transmission theoretically by means of computational method—numerical simulation. Hopefully, exploring the influence on the light behavior in the nanostructures through the theoretical simulation can provide a better understanding of the beam propagation phenomena for the relevant researchers. As an example, we studied the case of 200 nm thickness Ag film coated on quartz substrate and designed a structure with corrugation of one thoroughly-penetrated central slit and 16 grooves on the exit side. The 16 grooves having dimension of 80 nm in depth and 200 nm in width are symmetrically distributed around the central slit, as shown in Figure 11.²⁶ For the grooves with the aspect ratio

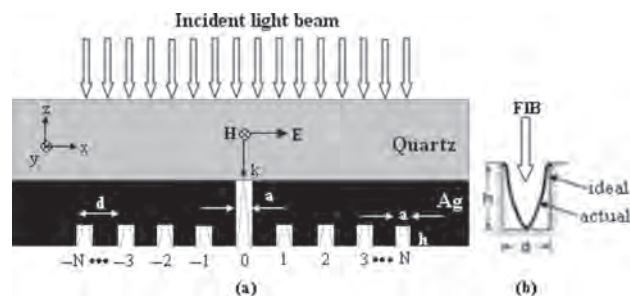


Fig. 11. Design configuration of the enhanced plasmonic nanostructure. (a) Side view of the designed structure. The grooves in the corrugation have the same depth and width. The dotted line in the grooves means the actual shape after the FIBM. Period of the corrugation is $d = 500$ nm. (b) Schematic diagram of FIBM induced V-shape for the nanostructures with high aspect ratio.

of 2.5, the final bottom width of the grooves after the FIBM is empirically estimated to be ~ 150 nm.

It is demonstrated by our simulation results that the sharp V-shaped central slit plays a positive dominant role in transmission to a large extent. It helps improving beam shaping significantly. The V-grooves cause a red-shift of the peak wavelength and broadening of the cut-off wavelength in transmission along the propagation direction due to the shape resonance.²⁸ Moreover, it causes beam diverging in the far-field region. Thus it plays a negative role in the propagation process. However, the influence from the V-grooves on the transmission spectrum can be ignored in the mixture case of both the V-shaped central slit and grooves existing. As a matter of fact, the sharp edge of the slit/grooves with small size, e.g., $d_2 = 25$ nm, is difficult to be intentionally directly milled using the FIBM. However, it is possible to be formed naturally due to the inherited characteristics of the FIBM.

The V-shape effect is not limited only for the FIBM. Some other techniques such as e-beam lithography, also has the V-shaped structuring effect while the exposed pattern transferred from the PMMA resist to substrate. Therefore, the simulation results are also applicable for other nanofabrication techniques.

In addition, for nanofabrication using focused ion beam (FIB) technique, Ga^+ implantation will be a negative factor that will change dielectric constant of the scanned substrate or thin films.²⁹ Normally, for FIB milling under 30 keV ion energy, induced ion implantation depth is 30 nm distributed at subsurface. Of course, optical performance will be varied accordingly. For more information, please read the relevant papers.

2.4. Funnel-Shaped Array for Superfocusing

A funnel-shaped array of single Ag nano-cylinders is proposed on the basis of transmission characteristics of single noble nano-cylinders.³⁰ Computational numerical study is carried out by means of FDTD algorithm for analysis of the electromagnetic field propagation at the facet of the “funnel” as well as coupling effect between the localized SP waves and the metal nanocylinders. It demonstrates that super-focusing at near-field ranges has been realized through such a structure.

Figure 12 shows the top view of the proposed funnel-shaped waveguide. The structure consists of two-pathway Ag nanocylinders array with the gradually changed diameters and discrete spacing forms the funneled-shaped waveguide with nano-scale dimension. The surrounding medium is simply set to be air. The geometrical parameters of the Ag nanocylinder array are denoted with the radius R and the transmission length D from the incident position to the funneled facet, the arm length L , the funnel obliquity θ , and the focus field width d , were denoted respectively in Figure 12. Finite-difference and time-domain (FDTD)

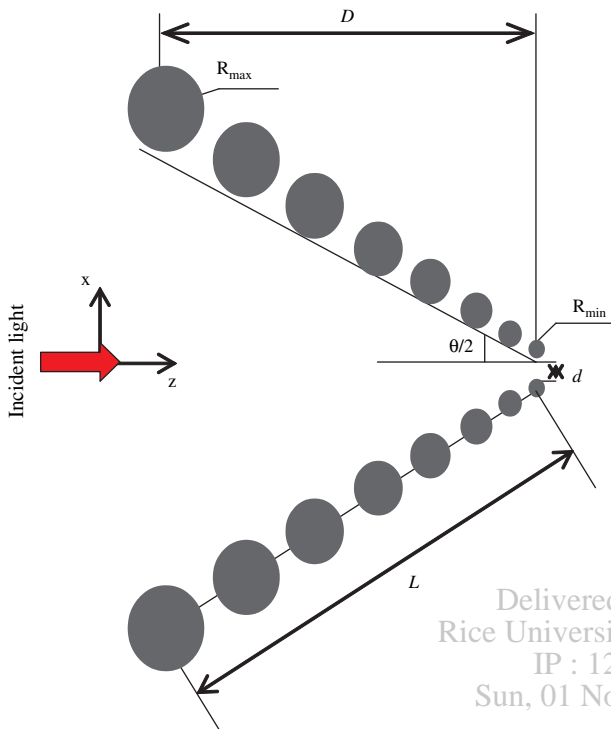


Fig. 12. The top view of the funnel-shaped waveguide with diameter gradually changed and discretized metal nanocylinders.

simulations demonstrated that the proposed structures with different spacing and funnel angles have versatile light propagation characteristics. These structures can focus the incident Gaussian light beam (200 nm at its full width at half maximum (FWHM)) into beam sizes of 10 nm, 15 nm, and 20 nm, respectively, which correspond to the transmission efficiencies of 38%, 40%, and 80%. These simulation results imply that the SP-based discrete array with the metal nanowire may make some nanophotonic devices such as high-intensity SP source, biophotonics etc. into reality in the near future.

In addition, coupling mode-based nanophotonic U-shaped logic circuit binary devices can be designed on the basis of SPP wave. Coupling of TM mode between adjacent air channels on metal and propagation of surface plasmon polaritons (SPPs) wave is studied.³¹ Different output intensity were obtained by modify the U-shaped air channel width, and logical binary “1” or “0” is gotten after decision threshold. The coupling mode theory is used to explain the simulation results, they consistent with each other well. The structure can used to obtain all four binary arrays applying to high integrated logical circuit.

3. PLASMONIC STRUCTURES FOR ANTENNA

Compact directive antennas with a single feeding point are highly attractive in practice. Parabola has the property of high directivity. However, parabola is quite bulky to

restrict its applications in some special applications. Conventional patch antenna has simple feeding mechanisms, whereas its radiated pattern is affected by the surface wave and has low gain. On the other hand, patch array antenna can offer the directive feature, but the complex feeding mechanism and the radiation efficiency limit its application range. Therefore, high directive antenna with more compact structure and simple feeding is of great interest in recent years.

3.1. Electromagnetic Band-Gap Structures-Based Antennas

Recently the electromagnetic band-gap (EBG) structures have been widely studied in the electromagnetic and communication antenna applications.^{32–37} EBG structures are artificial units composed of metallic patches arrays, which are periodically printed on a dielectric substrate and connected to the metallic ground plane with vias. The structures have frequency band-gap feature, which is revealed in two important ways: the suppression of surface-wave propagation⁵ and the in-phase reflection coefficient. The feature of surface-wave suppression can be applied to patch antenna designs to improve antenna’s radiation performance and reduce the mutual coupling of the array elements.^{37, 38} Meanwhile, the feature of in-phase reflection coefficient can be lead to low profile antenna designs.^{39–41} A patch antenna and microstrip method (PAMM) was reported for the purpose of identifying the surface-wave band-gap range.^{42, 43} The key idea of PAMM is that a patch antenna, fed by a microstrip line, is served for a radiator and an open-end microstrip line with characteristic impedance of 50 Ω , is employed as a detector for the electromagnetic field along the substrate, as shown in Figure 13. The surface-wave is excited by a microstrip patch antenna, which is different with open-ended microstrip line (used in Ref. [33]). The patch

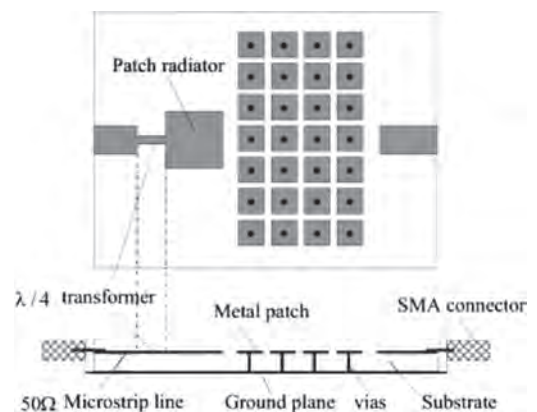


Fig. 13. Sketch of the experiment setup of PAMM. SMA is utilized to be connected easily to the network analyzer. Reprinted with permission from [42], H. Xu et al., *Microw. Opt. Technol. Lett.* 49, 2668 (2007). © 2007, IEEE.

antenna is a square metal patch, which has the size of $6.7 \text{ mm} \times 6.7 \text{ mm}$ and the resonant frequency is 13.55 GHz . Several rows of EBG structures are inserted between the detector and the radiator. The band-gap range of surface-wave can be identified by measuring the transmission through the detector and the radiator. Simulation results show that the transmission coefficient with EBG presence is lower than that of case without EBG absence above 10 dB . On the other hand, the gain of the antenna increases 1.9 dB when four rows of EBG are present. The results verify that the propagation of surface-wave is suppressed and the method is effective.

The other type of metamaterial superstrate antenna with high directivity is introduced for the Ku-band ($12\text{--}18 \text{ GHz}$). The device has a simple feeding source made from a co-plane EBG structure patch antenna.⁴⁴ The metamaterial, which consists of metallic grids and foam slices, is used to simulate a low refractive index homogeneous medium and placed in front of the feeding source. The simulation results show that the gain of the metamaterial antenna is improved to about 21.6 dB at 14.6 GHz and the antenna directivity is enhanced obviously. A schematic view of the antenna is presented in Figure 14. Metamaterial is made of two-layer metallic grids and foam slices ($\epsilon_r = 1.07$ at 10 GHz). Metamaterial superstrate is placed above the EBG substrate with a perfect electronic conductor (PEC) backing plate. A patch antenna surrounded with several rows of mushroom-like EBG structures is served as the radiation source, which can enhance the patch radiation efficiency and reduce the antenna height. The mushroom-like EBG structure consists of four parts, which are: (1) a ground plane, (2) a dielectric substrate, (3) square metal patches, (4) connecting vias, as shown in Figure 15. The frequency band-gap is determined by the patch width w , the gap size g , the substrate thickness t and the substrate dielectric constant ϵ_r . In theory, the maximum directivity of an aperture antenna is $D_{\max} = 4\pi A/\lambda_0^2$, and the maximum gain $G_{\max} = kD_{\max}$, k is the efficiency. Given $k = 1$, the theoretical value of the maximum gain is $G_{\max}(\text{dB}) = 10\log(4\pi A/\lambda_0^2)$. Here the area of the aperture is $A = 116 \text{ mm} \times 116 \text{ mm}$, and $\lambda_0 = c_0/f_0 = 20.55 \text{ mm}$ (14.6 GHz), therefore the maximum gain is $G_{\max}(\text{dB}) = 25.9 \text{ dB}$. The simulated result is $G = 21.6 \text{ dB}$, which has approached the theoretical limitation. If the aperture size of the metamaterial superstrate is larger than that of our simulation, the higher directivity can be obtained.

3.2. Waveguide Slit Array Antenna

Most recently, a waveguide slit array antenna with high gain and narrow beam width was reported by Huang et al.⁴⁵ This antenna is formed by subwavelength slits surrounded with periodic grooves, as shown in Figure 16, in which a narrow slit replaces a long slit, and a rectangle waveguide replaces the corresponding excitation of

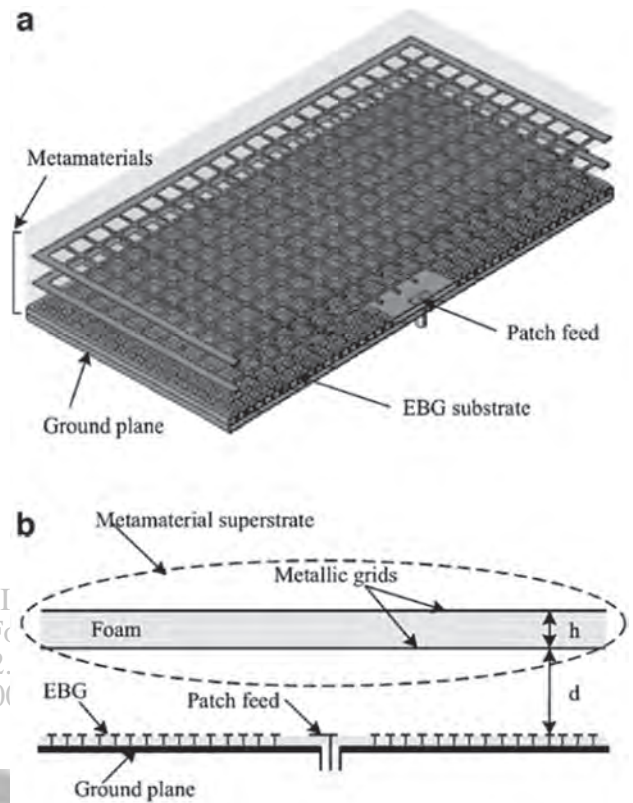


Fig. 14. High directivity antenna combined with a patch source surrounded with EBG structure and a slab metamaterial superstrate: (a) cut-away drawing of the antenna and (b) cross section representation of the antenna. Reprinted with permission from [43], H. Xu et al. *Int. J. Infrared Mili. Waves* 29, 493 (2008). © 2008, IEEE.

the plane wave. The far field radiation characteristics of the improved antenna are investigated. The physical mechanism for the performance improvement is governed by the resonance excitation of surface electromagnetic waves and can be well described by the coherent superposition of power radiated from the grooves and central slits. The

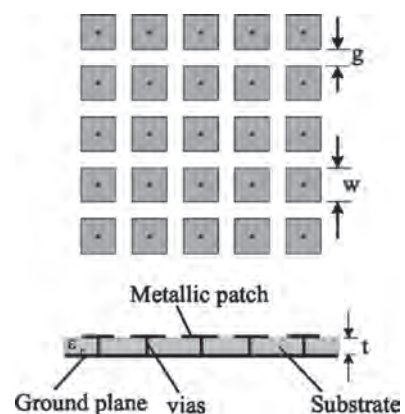


Fig. 15. Geometry of the mushroom-like electromagnetic band-gap structures. Reprinted with permission from [43], H. Xu et al., *Int. J. Infrared Mili. Waves* 29, 493 (2008). © 2008, IEEE.

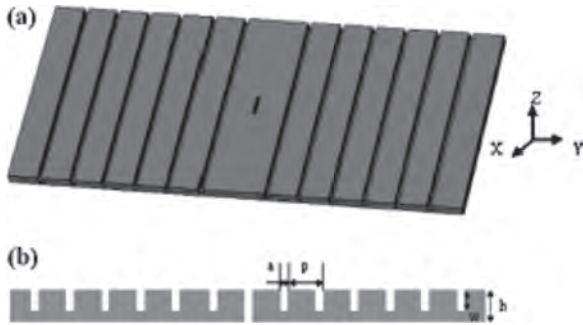


Fig. 16. (a) The model of the waveguide slit antenna integrated with periodic grooves and (b) a cross section of the periodic corrugated structure. Reprinted with permission from [45], C. Huang et al., *Appl. Phys. Lett.* 91, 143512 (2007). © 2007, American Institute of Physics.

finite grooves are symmetrically distributed at both sides of the narrow slit, and their detailed parameters are determined as follows: period $p = 20$ mm, depth $w = 3.6$ mm, width $a = 2.8$ mm, and number $N = 6$. This antenna is designed to work at 13 GHz. The gain and angular width of the half-power beam of this proposed antenna are compared with the conventional slit array antenna using the FDTD method. It has been demonstrated that the gain of the proposed antenna surrounded with periodic grooves can be improved by 11 dB, and the beam angle is confined to the normal direction. The mechanism for the improvement of the radiation pattern has been explained by the resonance excitation of the surface EM wave and coherent superposition of power radiated from the grooves and central slits. Moreover, it is believed that this antenna will have potential applications in such wireless communication and point to point communication due to its low cost, light weight, and low profile.

4. METALLIC NANOPARTICLES ARRAY FOR BIOSENSING

Metallic nanoparticles array for biosensing is a major application of nanophotonic devices, especially the localized surface plasmon resonant (LSPR) effect-based nanobiosensors. It is an important approach for immunoassay. Numerous biosamples can be detected by means of the LSPR-based nano-biosensors such as biotin,⁴⁶ amyloid-derived diffusible ligands,⁴⁷ and *Staphylococcus aureus* enterotoxin B etc.⁴⁸ It becomes appealing for biological researchers due to its advantages of portable, cost effective, light weight, small volume, and simple system in comparison to the conventional SPR system, e.g., Bicore system.

4.1. Design Methods

4.1.1. Discrete Dipole Approximation Algorithm-Based Calculation

Discrete dipole approximation (DDA) is one of the most efficient numerical methods for nanoparticles of arbitrary

shape. DDA can calculate the absorbing and scattering of the arbitrary shape and dimension. This method has strong advantages of using less calculated resource, calculating the mutual action between the light and the metal nanoparticles with arbitrary shapes. It expresses the target particles as an array of point dipoles, with the fields of these dipoles determined self consistently. Any particles can be divided into a large number of polarizable cubes (point dipoles), and the electromagnetic scattering problem is solved essentially exactly as long as the cubes are small enough and subject to a model for the cube polarizability.

In the present applications using an extended DDA, we modeled the rhombic structure of the particles accurately. This work aimed the problems of recent experiments that were the parameters of the rhombic sliver nanoparticle arrays could not be decided only by the experiment facture and we will show that the results are in quantitative agreement with experiments. The theory for determining the parameters in the fabrication of the rhombic silver nanoparticle array is provided. The DDA program DDSCAT 6.1⁴⁹ is from Draine and Flatau, the dielectric constants for silver are from Ref. [50]. In order to ensure the effect of the substrate is included in the result, we considered it as the effective index of medium in calculation, which is 1.2⁴⁹ and the wavelength values in the parameter file should be changed too. The size of the dipole is 2 nm which can promise the perfect convergence of the calculated results and the higher calculated efficiency.⁵⁰

The DDA simulation parameters are determined by the experiment. As shown in Figure 17, the Ag nanorhombus has in-plane width of ~ 140 nm and out-of-plane height of ~ 40 nm. The angle of the arris and underside is 60° and the period of the Ag nanorhombus array is 440 nm. Considering the index of air and glass substrates to be a uniform index, the refraction index around the Ag nanorhombus array used in the simulation was determined. This Ag nanorhombus lies in $y-z$ plane and the direction of the incident light is x -axis. The polarization of the incident light is y -axis.

In computation calculations, for the same period and in-plane widths with different out-of-plane heights can be

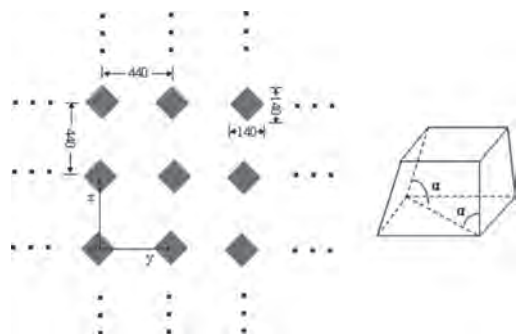


Fig. 17. The parameters of the DDA computational numerical simulation.

fabricated by depositing metal with different thicknesses through the masks using thermal or electron beam evaporation. The calculations were done with particles arranged in rhombic structure, however, there are different thicknesses in the fabrication, so an important problem is what effect that this different thickness lead to the results. To study this effect, we have calculated the spectrums of different thicknesses. In these calculations, each particle is displaced relative to its position on a perfect rhombic array. The thicknesses of rhombic structure are 25 nm, 30 nm, 35 nm, 40 nm, 45 nm, 50 nm, 55 nm and 60 nm respectively.

Figure 18(a) shows the results of the DDA simulation, where

(1) presents the extinction spectrum of the DDA simulation whose thickness is equivalent to 25 nm;

(2) corresponds to the extinction spectrum when the thickness is changed to 30 nm;

(3) shows the extinction spectrum for Ag nanoparticles whose thickness is 35 nm and the extinction spectrums with the thicknesses of 40 nm, 45 nm, 50 nm, 55 nm and 60 nm are illustrated by (4), (5), (6), (7), (8) respectively.

The positions of the peaks are located in 579.84 nm, 589.85 nm, 599.86 nm, 609.88 nm, 619.89 nm and 629.91 nm. The relationship between the peaks of wavelength and the thicknesses of rhombic silver particles is shown in Figure 18(b) which shows the effect of thicknesses to the positions of the peaks. The relationship between the extinction efficiency of wavelength and the thickness of rhombic silver particles is shown in Figure 18(c). Considering the full width at half maximum (FWHM) of the wavelength and the use for the biochip which mainly used the redshifts of the peaks of wavelength of nanostructure, the perfect thickness is 35 nm~45 nm for the experiment. The preferable thickness of fabrication is 40 nm.

The diverse diameters of the polystyrene spheres (PS) are used to adjust the period of the rhombic silver particles. The correct direction for the facture of the rhombic silver particles array is offer by calculating the effects of the periods. The periods of rhombic structure are 340 nm, 380 nm, 420 nm and 460 nm respectively. The positions of the peaks are located in 588 nm, 597 nm, 604 nm and 608 nm. When the periods of the rhombic silver particles are different, the positions of the peaks are also changed. Figure 19(a) shows the resulting spectra, which look very similar to each other. However there are two significant differences between them. First, the peak heights of the small periods are always higher than those of the large periods. It is easy to be understood as coherence of the dipole sums is expected to be the same area. The second effect is that positions of the peaks are less strongly red shifted when the periods becomes larger. The relationship between the peaks of wavelength and the period of rhombic silver particles is shown in Figure 19(b),

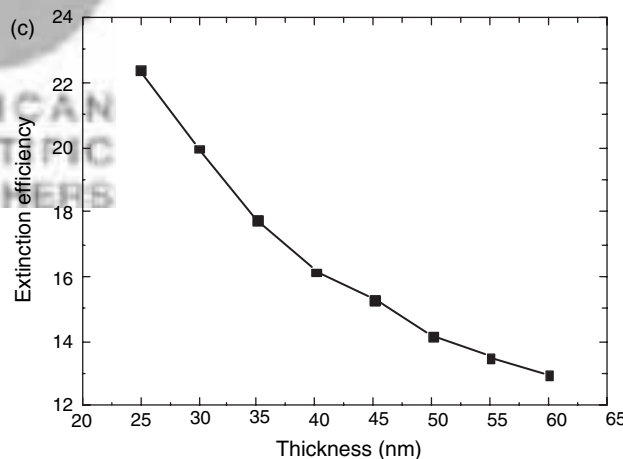
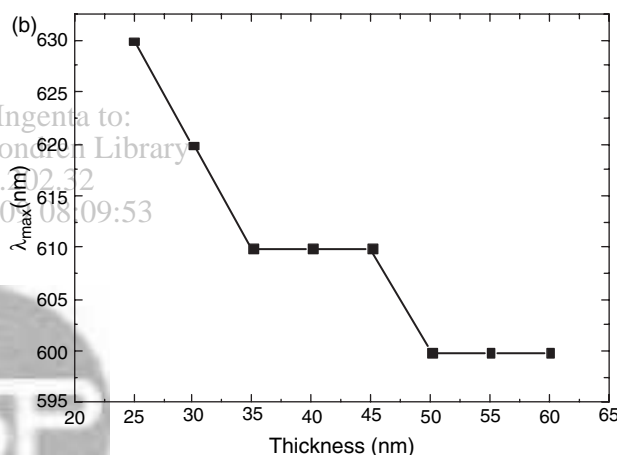
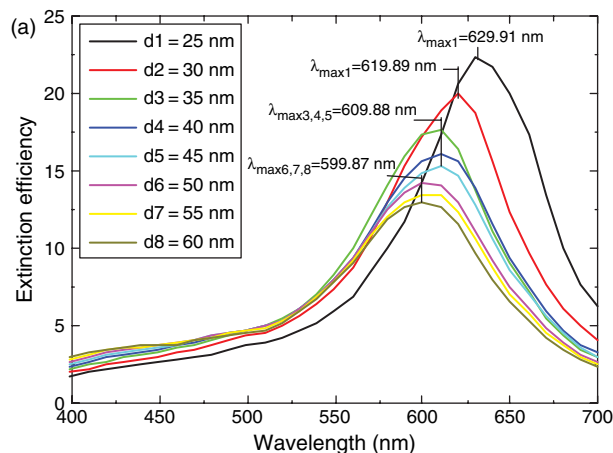


Fig. 18. (a) Extinction spectra of rhombic silver particle array for different thickness. (b) Relationship between the peaks of wavelength and the thicknesses of rhombic silver particles. Relationship between the extinction efficiency of wavelength and the thicknesses of rhombic silver particles.

where the first point stands for the single particle when the period is 0. The relationship between the extinction efficiency of wavelength and the period of rhombic silver particles is shown in Figure 19(c). Considering the FWHM

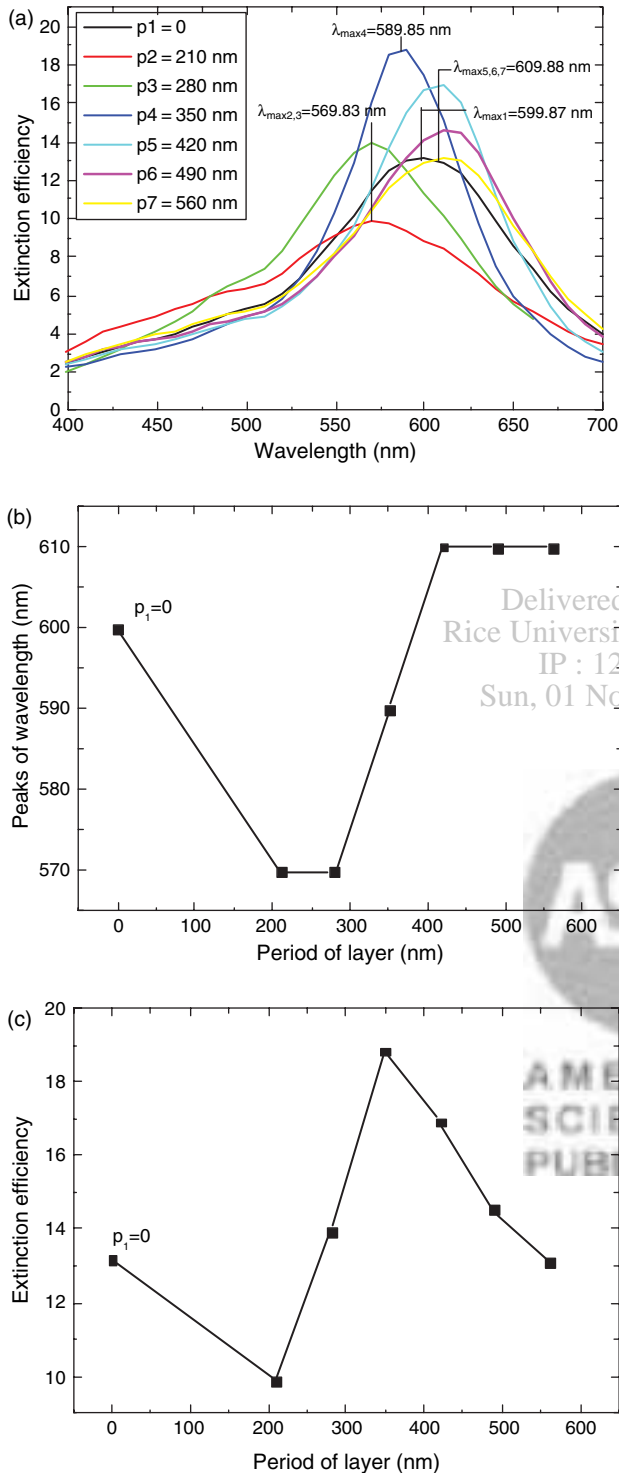


Fig. 19. (a) Extinction spectra of rhombic silver particle array for different periods. (b) Relationship between the peaks of wavelength and the periods of rhombic silver particles. (c) Relationship between the extinction efficiency of wavelength and the periods of rhombic silver particles.

and the intensity of the extinction efficiency, the perfect periods are 350 nm~560 nm. The period of fabrication is 440 nm. Fabrication and biosensing experimental results can be seen from Refs. [51–53].

4.1.2. Finite-Difference and Time-Domain Algorithm-Based Design

Finite-difference and time-domain (FDTD) algorithm treats Maxwell equations as a set of finite difference equations in both time and space. The model space considered includes both the probe and the sample surface and consists of an aggregation of cubic cells with each cell having its own complex dielectric constant. The finite difference equations can be written as:

$$\begin{aligned} & \frac{H_{z(t;x,y+\Delta y,z)} - H_{z(t;x,y-\Delta y,z)}}{2\Delta y} - \frac{H_{y(t;x,y,z+\Delta z)} - H_{y(t;x,y,z-\Delta z)}}{2\Delta z} \\ &= \tilde{\epsilon}(x,y,z) \frac{E_{x(t+\Delta t;x,y,z)} - E_{x(t-\Delta t;x,y,z)}}{\Delta t} \\ & \frac{H_{x(t;x,y,z+\Delta z)} - H_{x(t;x,y,z-\Delta z)}}{2\Delta z} - \frac{H_{z(t;x+\Delta x,y,z)} - H_{z(t;x-\Delta x,y,z)}}{2\Delta x} \\ &= \tilde{\epsilon}(x,y,z) \frac{E_{y(t+\Delta t;x,y,z)} - E_{y(t-\Delta t;x,y,z)}}{\Delta t} \\ & \frac{H_{y(t;x+\Delta x,y,z)} - H_{y(t;x-\Delta x,y,z)}}{2\Delta x} - \frac{H_{x(t;x,y+\Delta y,z)} - H_{x(t;x,y-\Delta y,z)}}{2\Delta y} \\ &= \tilde{\epsilon}(x,y,z) \frac{E_{z(t+\Delta t;x,y,z)} - E_{z(t-\Delta t;x,y,z)}}{\Delta t} \end{aligned} \quad (6)$$

where $\mathbf{E} = \mathbf{E}(E_x, E_y, E_z)$ and $\mathbf{H} = \mathbf{H}(H_x, H_y, H_z)$ are the electric field and the magnetic induction vectors, respectively, and $2\Delta x$, $2\Delta y$, $2\Delta z$ are increments along the three coordinate directions respectively, Δt is the unit time increment, and $\tilde{\epsilon}(x, y, z)$ is the complex dielectric constant of the medium at that point. Equation (6) is simultaneously solved to determine the component values at the time $t + \Delta t$. A commercial professional software was adopted here for the computational calculation and numerical analysis. The used metal here is Ag with $\epsilon_m = -17.24 + i0.498$ at the wavelength of 633 nm, and $\epsilon_d = 1.243$ for SiO_2 . Broad band of the incident light is ranging from 400 nm to 750 nm with plane wave in normal incidence angle $\theta = 0^\circ$. Meshing size in x and y (two-dimensional simulation) is $\Delta x = 2$ nm and $\Delta y = 2$ nm, respectively. Simulation time t (theoretically, $t = \Delta x/2c$, c is the velocity of light) is set to be 125 fs. The output result is extinction spectrum.

Here we set hybrid Au–Ag nanoparticles as a design example to illustrate the FDTD-based design approach.⁵⁴ By-products of the pure Ag nanoparticles are oxidation and sulfuration (further study is required to reveal that which process is more significant) which will change dielectric constant of the Ag particles, and transmission property will degrade accordingly. To solve this problem, we put forth a new structure here, hybrid Au–Ag metallic nanoparticles array with Au thin film covered on the Ag film surface. Therefore, the Au film acts as both a protector and modulator here. On the one hand, it can protect Ag film surface from oxidation. On the other hand,

it can modulate the transmission property of the nanosensors so as to achieve higher detection sensitivity. Using a finite-difference and time-domain (FDTD) algorithm, we designed the extinction spectra and the corresponding electric fields at the extinction spectra peak position of the hybrid nanoparticles.

The hybrid Au–Ag triangular nanoparticles were proposed as a sensitive cell of the LSPR-based nanobiosensor. Using FDTD algorithm, we designed and calculated the extinction spectra as well as the corresponding electric field of the hybrid nanoparticles array. Three-dimensional geometrical model of the hybrid Au–Ag triangular nanoparticles array is shown in Figure 20.

Out-of plane height of the silver nanoparticles is 50 nm and the upper Au nanoparticles is 5 nm, and the in plane widths of each nanoparticles is 100 nm. The period of the nanoparticle array is 400 nm and wavelength of the incidence white light source is ranging from 400 nm to 700 nm. The incidence light beam is projected in perpendicular to the substrate. In order to investigate the transmission property of different refractive index of the mediums surrounding this hybrid nanoparticles, we selected the mediums of air ($n_1 = 1.0$) and Protein A (Protein A: PBS (0.01 M, pH 7.4) = 1:100, $n_2 = 1.3352$) surrounding the nanoparticles. When the refractive indexes of the surrounding mediums are 1.0 and 1.3352, the computational results using FDTD method are shown in Figure 21. From the result, we can obtain sensitivity of the hybrid Au–Ag triangular nanoparticles as $S = (\lambda_{\max 1} - \lambda_{\max 2}) / (n_2 - n_1) = (551.638 - 484.513) / (1.3352 - 1.0) = 200 \text{ nm/RIU}$. Thus it is reasonable to believe that the hybrid nanoparticles can realize the higher sensitivity detection of biomolecules.

In addition, we calculated the electric fields when the incident light wavelength is equal to the LSPR wavelength λ_{SPP} . The electric fields can be expressed as $\mathbf{E}^2 = \mathbf{E}_x^2 + \mathbf{E}_y^2 + \mathbf{E}_z^2$. Using the FDTD algorithm, we

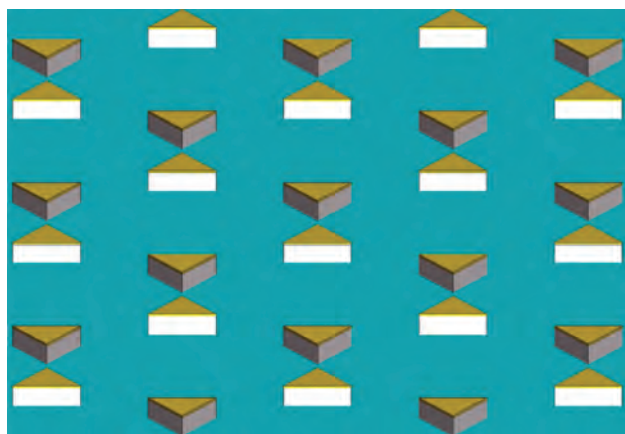


Fig. 20. Schematic diagram of the model of the hybrid Au–Ag triangular nanoparticles array.

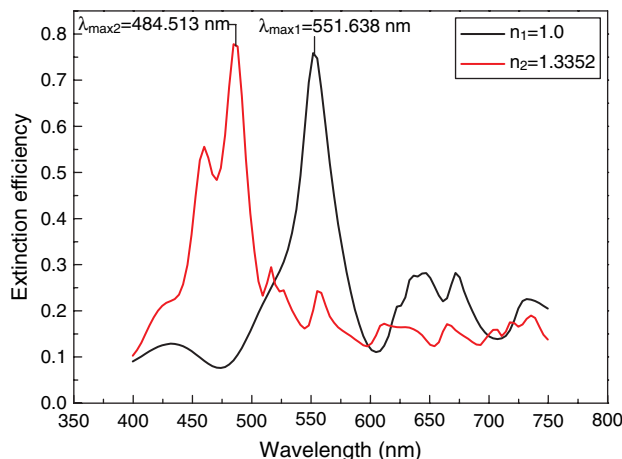


Fig. 21. FDTD solution calculated result when the refractive index medium surrounding this hybrid nanoparticles are 1.0 and 1.3352, respectively.

obtained the electric field \mathbf{E} when the incident light wavelength is $\lambda_{\text{in}} = 551.638 \text{ nm}$ (refractive index of the medium surrounding this hybrid nanoparticles is $n_d = 1.0$). The electric field is also calculated when $\lambda_{\text{in}} = 484.513 \text{ nm}$ (refractive index of the medium surrounding this hybrid nanoparticles is $n_d = 1.3352$). Figure 3 shows the calculated results of the electric field for the case $\lambda_{\text{in}} = \lambda_{\text{SPP}}$. It can be seen from Figures 22(a) and (b) that when the refractive index of the medium surrounding the hybrid nanoparticles is $n_d = 1.0$, the total electric field \mathbf{E} from Au surface in 5 nm thickness changed tremendously as well. These results indicated that the hybrid Au–Ag triangular nanoparticles can function as a platform for detecting the biomolecules such as Protein A.

A typical protein can directly bind to the surface of Au film. Using our developed LSPR-based nanobiosensor with the hybrid Au–Ag nanoparticles, we can realize the refractive index sensitivity of 200 nm/RIU. The nano-biosensors demonstrate the potential applications in monitoring, detection and identification of biological agents, as well as characterization of intermolecular interactions.⁵⁴

4.1.3. The Multiple Multipole Program Algorithm-Based Design

The multiple multipole program (MMP) a semi-analytic method for numerical field computations that has been applied to electromagnetic fields and to acoustics.^{55, 56} Essentially, the field is expanded by a series of basis fields. Each of the basis field is an analytic solution of the field equations within a homogeneous domain. The amplitudes of the basis fields are computed by a Generalized Point Matching Technique that is efficient, accurate, and robust. The analysis of metallic nanoparticles with different

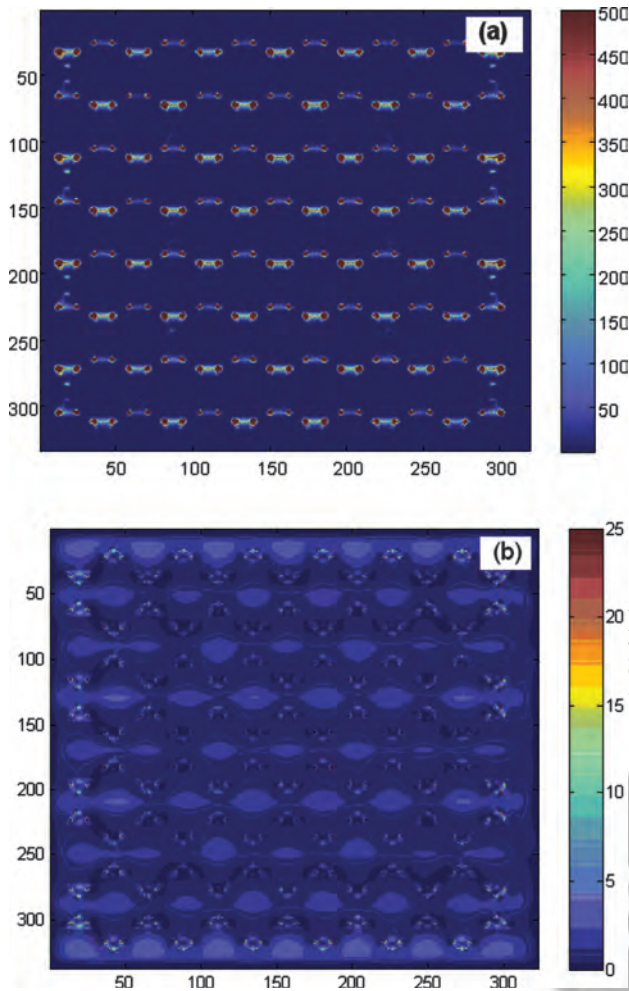


Fig. 22. FDTD solution calculated electric field result when the incidence light wavelength is equal to the LSPR wavelength. (a) Total electric field $\mathbf{E}^2 = \mathbf{E}_x^2 + \mathbf{E}_y^2 + \mathbf{E}_z^2$ from Au surface 5 nm; $n = 1.0$, $\lambda_{in} = \lambda_{max} = 551.638$ nm; (b) Total electric field $\mathbf{E}^2 = \mathbf{E}_x^2 + \mathbf{E}_y^2 + \mathbf{E}_z^2$ from Au surface 5 nm; $n = 1.3352$, $\lambda_{in} = \lambda_{max} = 484.513$ nm.

shapes such as spherical and triangle-shaped nanoparticles can be performed using the semi-analytical multiple multipole (MMP) method, which provides complex eigenvalue estimations as well as proper error measures. While controlling error measures highly-accurate computations are carried out especially for coupled-particle configurations with different inter-particle distances and under various illumination conditions. For more information regarding how to design the metallic nanoparticles, please read the textbook in Ref. [57]. Some design examples can be found in this book.

4.2. Nanofabrication

Considering integrality of this paper, a brief introduction of commonly used three fabrication techniques: focused ion beam milling, self-assembly monolayer, and laser interference lithography, is addressed here.

4.2.1. Focused Ion Beam Technique

Focused ion beam milling (FIBM) is a point-to-point scanning technique. Material sputtering effect can be formed while high energy of accelerated Ga^+ bombing the sample surface, and thus the material removal can be realized. Therefore, it is a pure physical process. Pattern transfer from photoresist into substrate for conventional photolithography and e-beam writing techniques is not necessary for the FIBM. Moreover, there is no substrate material selectivity. With development of the FIBM, some extra functions were invented such as chemical gas assistant etching and deposition. With these functions, some fine structuring process at local region can be realized by means of the FIBM, e.g., fine line joining, nanohole drilling, and nanoparticles forming etc.⁵⁸ It is a maskless technique. There is no shape limitation for the FIBM process because any two-dimensional pattern can be designed by users in advance and then call the patterns into the defined milling windows. For current commercial FIB machines, the feature size as small as several tens nanometers can be realized. However, it has drawbacks of high expenditure, slow speed, and small fabrication area. Therefore, it is more suitable to be used for fabrication of prototype and master piece.

4.2.2. Self-Assembly Monolayer

Self-assembly monolayer (SAM) also named nanospherical lithography (NSL), are surfaces consisting of a single layer of molecules on a substrate. Rather than having to use a technique such as chemical vapor deposition or molecular beam epitaxy to add molecules to a surface (often with poor control over the thickness of the molecular layer), self assembled monolayers can be prepared simply by adding a solution of the desired molecule onto the substrate surface and washing off the excess.

As an example, fabrication of rhombic Ag particles using SAM is introduced here. SAM is employed to create the surface-confined rhombic Ag nanoparticles supported on a glass substrate.^{46,49} This method is developed on the basis of the NSL technique.⁵⁷ At first, the glass substrate was cleaned in a piranha solution (1:3 30% $\text{H}_2\text{O}_2/\text{H}_2\text{SO}_4$) at 80 °C for 30 min., and then cooled by high-pressure N_2 gas. Once cooled, the glass substrates were rinsed with copious amounts of second distilled water and then sonicated for 60 min. in 5:1:1 $\text{H}_2\text{O}/\text{NH}_4\text{OH}/30\% \text{H}_2\text{O}_2$. Next, the single-layer of size-monodispersed (the sphere size of the chemical solutions which is spin-coated as a monolayer determines the generated rhombic particle size) polystyrene nanospheres (PS, 500 nm, 2%) and glass nanospheres (GS, 200 nm, 1%) with fluorocarbon surfactant (FSO) (100:1000:1 PS/GS/FSO) solution $\sim 10 \mu\text{l}$ were coated onto the glass substrate to form a deposition mask, and then followed by hydrofluoric acid etching to remove the glass nanospheres. After that, the Ag metal thin film

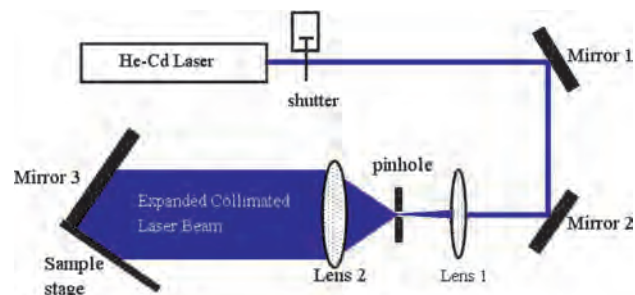


Fig. 23. Experimental setup of the Lloyd's mirror laser interference lithography system.

was deposited through the nanosphere masks using thermal evaporation or electron beam evaporation. After removal of the polystyrene nanospheres by sonication in absolute ethanol for 3 min., well ordered two-dimensional (2D) rhombic Ag nanoparticles array was finally obtained on the substrates. By modulation of the nanosphere diameter and the deposited Ag film thickness, the nanoparticles with different in-plane widths, out-of-plane heights, and interstructure spaces can be tuned.

4.2.3. Laser Interference Lithography

A Lloyd's mirror interferometer system was built, as shown in Figure 23.⁶⁰ Light source is He-Cd laser with 442 nm working wavelength. The laser beam is filtered and expanded by a spatial filter which is composed of Lens 1 and a pinhole. The expanded beam is collimated by Lens 2. A part of the incident beam is reflected back by the mirror which is positioned in normal to the substrate and interferes with the other non-reflection beam to form the interference patterns. Since the beam is only split with a short path length near the substrate, this setup is very insensitive to the mechanical vibration caused instabilities. Hence no extra feedback control system is required to stabilize the interference fringe patterns.⁶¹

As a fabrication example, the formation of particles in photoresist spin-coated on quartz substrate is presented. Firstly, the quartz substrate is dipped in nitric acid solution for ~6 h. Then it is cleaned by ultrasonic vibrations and acetone to remove the dust attached on surface of the substrate. We use an oven baking the substrate for half an hour at 150 °C for the purpose of removing the solvent absorbed on the surface. After that, an etched mask layer of Cr with ~10 nm in thickness is deposited in the front side of the cleaned quartz. The Cr thin layer coated on the substrate is for the purpose of enhancing adhesion between photoresist and substrate, and can also be used as a protection layer for the dry etching in next step. On top surface of this Cr layer, a layer of positive resist (AR-P3170, Allresist Co.) with a thickness of 100 nm is spin-coated, and followed by pre-baking time of 20 min. at 95 °C. The dimension of the exposed area strongly depends on the exposure dose. Because of the cosine instead of rectangular distribution of

the exposure intensity, energy at wings or tails of the beam profile still has contribution on the exposure process. The wing energy causes line broadening at edge of the dots, and thus makes the dots dimension enlarged to a certain extent. Generation of the structures with high aspect ratio will be limited due to this broadening effect accordingly. For compensation, the corrected exposure time should be slightly shorter than the normal value. The photoresist was exposed by the collimated beam from the Lloyd's mirror interferometer system. A 1D grating pattern of the photoresist layer was formed after the first time exposure and development. Exposure dose was measured to be 1.5 mW/cm² in normal incidence. The developer adopted in our experiments is AR 300-35 (Allresist Co.).

5. SUMMARY

In summary, plasmonic structures for imaging and super-focusing is a new approach besides the concept of negative refractive index. It is possible to realize imaging resolution beyond diffraction limit with a certain working distance within several wavelengths range. To realize this target, one of technical challenges is that how to transfer the high spatial frequency near-field signals from evanescent wave to propagation wave. The other challenge is that how to amplify the near-field evanescent wave from conventional ~200 nm to be ~1 μm or even several wavelengths in free space.

Antenna design based on plasmonic structures is a new branch recently. Not only the design of the communication antenna, the surface plasma-based antenna (also called optical antenna) design theory can be also used as wavelength scaling.⁶² Optical antennas are likely to be employed for boosting the efficiency of light-matter interactions in a wide range of settings, such as photovoltaics and light-emitting devices.

LSPR-based nano-biosensing is another hot topic in the fields of both nano-optics and biomedicine recently. This new LSPR-based nano-biosensor with rhombic Ag nanoparticles array presents a detection approach with higher sensitivity compared with the previously reported triangle Ag particle. However, theoretically, Mie theory was created for the particles with shapes of circular and ellipse only. The theoretical model for the nanoparticles with complicated shapes such as triangular, pyramid, rhombic, and five star etc., has not be developed so far to explain various physical phenomena quantitatively and qualitatively. It is crucial for essentially understanding and revealing the physical pictures inside the phenomena.

In addition, the LSPR-based sensing system is simple and cost effective compared to the SPR-based system. Therefore, it is reasonable to believe that the reported modified LSPR-based system will have a potential market in the next 5–10 years. Moreover, it may have significant advantages for some specific bio-samples immunoassay such as SEB, and ADDL etc.

Acknowledgment: The work was supported by the National Natural Science Foundation of China (No.60877021). The authors would like to thank Dr. Shaoli Zhu, Mr. Haofei Shi, Dr. Huiliang Xu, Mr. Cheng Huang, and Dr. Haiying Li for their contributions for the paper.

References

1. W. L. Barnes, A. Dereux, and T. W. Ebbesen, *Nature* 424, 824 (2003).
2. F. J. García-Vidal, H. J. Lezec, T. W. Ebbesen, and L. Martin-Moreno, *Phys. Rev. Lett.* 90, 213901 (2003).
3. F. J. García-Vidal, L. Martin-Moreno, H. J. Lezec, and T. W. Ebbesen, *Appl. Phys. Lett.* 83, 4500 (2003).
4. L. Martin-Moreno, F. J. García-Vidal, H. J. Lezec, A. Degiron, and T. W. Ebbesen, *Phys. Rev. Lett.* 90, 167401 (2003).
5. F. J. García-Vidal, H. J. Lezec, T. W. Ebbesen, and L. Martin-Moreno, *Phys. Rev. Lett.* 90, 213901 (2003).
6. Y. Fu, W. Zhou, L. E. N. Lim, C. Du, H. Shi, C. Wang, and X. Dong, *Appl. Phys. B* 86, 155 (2007).
7. Z. Sun and H. K. Kim, *Appl. Phys. Lett.* 85, 642 (2004).
8. D. Wu, N. Fang, C. Sun, and X. Zhang, *Appl. Phys. Lett.* 83, 201 (2003).
9. F. De Angelis, M. Patrini, Gobind Das, I. Maksymov, M. Galli, L. Businaro, L. C. Andreani, and E. Di Fabrizio, *Nano Lett.* 8, 2321 (2008).
10. N. Fang, Z. W. Liu, T. J. Yen, and X. Zhang, *Opt. Express* 11, 682 (2003).
11. N. Fang and X. Zhang, *Appl. Phys. Lett.* 82, 161 (2003).
12. N. Fang, H. Lee, C. Sun, and X. Zhang, *Science* 308, 534 (2005).
13. Z. Liu, N. Fang, T.-J. Yen, and X. Zhang, *Appl. Phys. Lett.* 83, 5184 (2003).
14. Z. Liu, H. Lee, Yi Xiong, C. Sun, and X. Zhang, *Science* 315, 1686 (2007).
15. H. Shi, C. Du, and X. Luo, *Appl. Phys. Lett.* 91, 093111 (2007).
16. H. Shi, C. Wang, C. Du, X. Luo, X. Dong, and H. Gao, *Opt. Express* 13, 6815 (2005).
17. Y. Yang, Y. Fu, S. Hu, S. Zhou, W. Yan, W. Chen, X. Cheng, and Z. Li, *J. Comput. Theor. Nanosci.* 6, 1030 (2009).
18. T. Xu, C. Du, C. Wang, and X. Luo, *Appl. Phys. Lett.* 91, 201501 (2007).
19. C. Wang, C. Du, Y. Lv, and X. Luo, *Opt. Express* 14, 5671 (2006).
20. Y. Fu, W. Zhou, L. E. Ng Lennie, C. Du, and X. Luo, *Appl. Phys. Lett.* 91, 061124 (2007).
21. Y. Fu, W. Zhou, and L. E. Ng Lennie, *Journal of Optical Society of America A* 25, 238 (2008).
22. Y. Fu, W. Zhou, and L. E. Ng Lennie, *Research Letter in Physics* 2008, 148085 (2008).
23. Y. Fu, W. Zhou, and L. E. Ng Lennie, *Appl. Phys. B* 90, 421 (2008).
24. Y. Fu and W. Zhou, *J. Nanophoton.* 3 (2009), in press.
25. Y. Fu and W. Zhou, *Plasmonics* 4, 141 (2009).
26. Y. Fu, W. Zhou, L. E. N. Lim, C. Du, H. Shi, and C. Wang, *Opt. Eng.* 45, 108001 (2006).
27. Y. Fu, W. Zhou, L. E. Ng Lennie, et al., *Appl. Phys. B* 86, 461 (2007).
28. Y. Fu, W. Zhou, and L. E. N. Lim, *J. Comput. Theor. Nanosci.* 4, 614 (2007).
29. Y. Fu and N. K. A. Bryan, *Appl. Phys. B* 80, 581 (2005).
30. Z. Xiu-Li, Y. Fu, W. Shi-Yong, P. An-Jing, and C. Zhong-Heng, *Chin. Phys. Lett.* 25, 3296 (2008).
31. X. Zhou, Y. Fu, K. Li, S. Wang, and Z. Cai, *Appl. Phys. B* 91, 373 (2008).
32. R. W. Ziolkowski and N. Engheta, *IEEE Trans. Antennas. Propagat.* 51, 2546 (2003).
33. P.-S. Kildal, A. A. Kishk, and S. Maci, *IEEE Trans. Antennas. Propagat.* 53, 2 (2005).
34. G. Cakir and L. Sevgi, *Microwave Opt. Technol. Lett.* 46, 399 (2005).
35. D. Stevenpiper, L. Zhang, F. J. Broas, N. G. Alexopoulos, and E. Yablonovitch, *IEEE Trans. Microwave Theory Technol.* 47, 2059 (1999).
36. P. de Maagt, R. Gonzalo, Y. C. Vardaxoglou, and J. M. Baracco, *IEEE Trans. Antennas. Propagat.* 51, 2667 (2003).
37. R. Coccioli, F. R. Yang, K. P. Ma, and T. Itoh, *IEEE Trans. Microwave. Theory. Technol.* 47, 2123 (1999).
38. F. Yang and Y. Rahmat-Samii, *IEEE Trans. Antennas. Propagat.* 51, 2936 (2003).
39. F. Yang and Y. Rahmat-Samii, *Microwave Opt. Technol. Lett.* 31, 478 (2001).
40. J. M. Bell and M. F. Iskander, *IEEE Antennas Wireless Propagat. Lett.* 3, 223 (2004).
41. A. P. Feresidis, G. Goussetis, S. H. Wang, and J. C. Vardaxoglou, *IEEE Trans. Antennas. Propagat.* 53, 209 (2005).
42. H. Xu, Y. Lv, X. Luo, and C. Du, *Microw. Opt. Technol. Lett.* 49, 2668 (2007).
43. H. Xu, Y. Lv, X. Luo, and C. Du, *International Journal of Infrared and Millimeter Waves* 29, 493 (2008).
44. F. Yang, EBG Structure and Reconfigurable Technique in Antenna Designs: Applications to Wireless Communications, Ph.D thesis, University of California, Los Angeles (2002).
45. C. Huang, C. Du, and X. Luo, *Appl. Phys. Lett.* 91, 143512 (2007).
46. S. Zhu, F. Li, X. Luo, C. Du, Y. Fu, *Sens. Actuat. B Chemical* 134, 193 (2008).
47. A. J. Haes, W. P. Hall, L. Chang, W. L. Klein, and R. P. Van Duyne, *Nano Lett.* 4, 1029 (2004).
48. S. Zhu, C. Du, Y. Fu, and A. Liu, *Sensors and Actuators B Chemical*, submitted.
49. B. T. Draine and P. J. Flatau (2004), User Guide for the Discrete Dipole Approximation Code DDSCAT.6.1 with the following website: <http://arxiv.org/abs/astro-ph/0409262>.
50. P. C. Chaumet, A. Rahmani, and G. W. Bryant, *Phys. Rev. B* 67 165404 (2003).
51. S. Zhu, X. Luo, C. Du, F. Li, S. Ying, Q. Deng, and Y. Fu, *J. Appl. Phys.* 101, 064701 (2007).
52. S. Zhu, F. Li, X. Luo, C. Du, and Y. Fu, *Opt. Mater.* 31, 769 (2009).
53. S. Zhu, F. Li, X. Luo, C. Du, and Y. Fu, *Nanomedicine* 3, 669 (2008).
54. S. Zhu, A. Liu, and Y. Fu, *Biomed. Microdevices* 11, 579 (2009).
55. C. Hafner, *J. Opt. Soc. Am. A* 12, 1057 (1995).
56. C. Hafner, X. Cui, A. Bertolace, and R. Vahldieck, *Proc. SPIE* 6617, 66170C (2007).
57. L. Novotny, B. Hecht (eds.), Principles of Nano-Optics, Cambridge University Press, The Edinburgh Building, Cambridge, UK (2006), Chap. 15, pp. 476–483.
58. Y. Fu, and N. K. A. Bryan, *J. Vac. Sci. Technol., B* 23, 984 (2005).
59. J. C. Hulthen and R. P. Van Duyne, *J. Vac. Sci. Technol. A* 13, 1553 (1995).
60. H. Li, X. Luo, C. Du, X. Chen, and Y. Fu, *Sensors and Actuators B Chemical* 134, 940 (2008).
61. C. J. M. van Rijn, *J. Microlith. Microfab. Microsyst.* 5, 0110121 (2006).
62. L. Novotny, *Phys. Rev. Lett.* 98, 266802 (2007).

Received: 30 September 2008. Accepted: 7 October 2008.